

Understanding the Emission and Morphology of the Unidentified Gamma-Ray Source TeV J2032+4130

R. ALFARO,¹ C. ALVAREZ,² J.C. ARTEAGA-VELÁZQUEZ,³ D. AVILA ROJAS^{id},¹ H.A. AYALA SOLARES^{id},⁴ R. BABU^{id},⁵
E. BELMONT-MORENO^{id},¹ K.S. CABALLERO-MORA^{id},² T. CAPISTRÁN^{id},⁶ A. CARRAMIÑANA^{id},⁷ S. CASANOVA^{id},⁸
U. COTTI^{id},³ J. COTZOMI^{id},⁹ S. COUTIÑO DE LEÓN^{id},¹⁰ E. DE LA FUENTE^{id},¹¹ C. DE LEÓN^{id},³ D. DEPAOLI^{id},¹²
N. DI LALLA^{id},¹³ R. DIAZ HERNANDEZ,⁷ B.L. DINGUS^{id},¹⁴ M.A. DUVERNOIS^{id},¹⁰ J.C. DÍAZ-VÉLEZ^{id},¹⁰ K. ENGEL^{id},¹⁵
T. ERGIN^{id},⁵ C. ESPINOZA^{id},¹ K.L. FAN^{id},¹⁵ N. FRAIJA^{id},⁶ J.A. GARCÍA-GONZÁLEZ^{id},¹⁶ M.M. GONZÁLEZ^{id},⁶
J.A. GOODMAN^{id},¹⁵ S. GROETSCH,¹⁷ J.P. HARDING^{id},¹⁴ S. HERNÁNDEZ-CADENA,¹⁸ I. HERZOG^{id},⁵ D. HUANG^{id},¹⁵
F. HUEYOTL-ZAHUANTITLA^{id},² P. HÜNTEMEYER^{id},¹⁷ A. IRIARTE^{id},⁶ S. KAUFMANN,¹⁹ J. LEE^{id},²⁰ H. LEÓN VARGAS^{id},¹
A.L. LONGINOTTI^{id},⁶ G. LUIS-RAYA^{id},¹⁹ K. MALONE^{id},²¹ J. MARTÍNEZ-CASTRO^{id},²² J.A. MATTHEWS^{id},²³
P. MIRANDA-ROMAGNOLI^{id},²⁴ J.A. MONTES,⁶ E. MORENO^{id},⁹ M. MOSTAFÁ^{id},²⁵ L. NELLEN^{id},²⁶ M. NEWBOLD^{id},²⁷
M.U. NISA^{id},⁵ R. NORIEGA-PAPAQUI^{id},²⁴ Y. PÉREZ ARAUJO^{id},¹ E.G. PÉREZ-PÉREZ^{id},¹⁹ C.D. RHO^{id},²⁸
D. ROSA-GONZÁLEZ^{id},⁷ E. RUIZ-VELASCO^{id},¹² H. SALAZAR,⁹ D. SALAZAR-GALLEGOS,⁵ A. SANDOVAL^{id},¹
M. SCHNEIDER^{id},¹⁵ J. SERNA-FRANCO,¹ A.J. SMITH^{id},¹⁵ Y. SON,²⁰ R.W. SPRINGER^{id},²⁷ O. TIBOLLA,¹⁹
K. TOLLEFSON^{id},⁵ I. TORRES^{id},⁷ R. TORRES-ESCOBEDO^{id},¹⁸ R. TURNER^{id},¹⁷ F. UREÑA-MENA^{id},⁷ E. VARELA^{id},⁹
L. VILLASEÑOR^{id},⁹ X. WANG^{id},¹⁷ ZHEN WANG,¹⁵ I.J. WATSON^{id},²⁰ S. YU,⁴ S. YUN-CÁRCAMO^{id},¹⁵ H. ZHOU^{id},¹⁸

(THE HAWC COLLABORATION)

¹*Instituto de Física, Universidad Nacional Autónoma de México, Ciudad de México, México*

²*Universidad Autónoma de Chiapas, Tuxtla Gutiérrez, Chiapas, México*

³*Universidad Michoacana de San Nicolás de Hidalgo, Morelia, México*

⁴*Department of Physics, Pennsylvania State University, University Park, PA, USA*

⁵*Department of Physics and Astronomy, Michigan State University, East Lansing, MI, USA*

⁶*Instituto de Astronomía, Universidad Nacional Autónoma de México, Ciudad de México, México*

⁷*Instituto Nacional de Astrofísica, Óptica y Electrónica, Puebla, México*

⁸*Instytut Fizyki Jadrowej im Henryka Niewodniczanskiego Polskiej Akademii Nauk, IFJ-PAN, Krakow, Poland*

⁹*Facultad de Ciencias Físico Matemáticas, Benemérita Universidad Autónoma de Puebla, Puebla, México*

¹⁰*Department of Physics, University of Wisconsin-Madison, Madison, WI, USA*

¹¹*Departamento de Física, Centro Universitario de Ciencias Exactas e Ingenierías, Universidad de Guadalajara, Guadalajara, México*

¹²*Max-Planck Institute for Nuclear Physics, 69117 Heidelberg, Germany*

¹³*Department of Physics, Stanford University: Stanford, CA 94305-4060, USA*

¹⁴*Los Alamos National Laboratory, Los Alamos, NM, USA*

¹⁵*Department of Physics, University of Maryland, College Park, MD, USA*

¹⁶*Tecnológico de Monterrey, Escuela de Ingeniería y Ciencias, Ave. Eugenio Garza Sada 2501, Monterrey, N.L., México, 64849*

¹⁷*Department of Physics, Michigan Technological University, Houghton, MI, USA*

¹⁸*Tsung-Dao Lee Institute & School of Physics and Astronomy, Shanghai Jiao Tong University, Shanghai, China*

¹⁹*Universidad Politécnica de Pachuca, Pachuca, Hgo, México*

²⁰*University of Seoul, Seoul, Rep. of Korea*

²¹*Physics Division, Los Alamos National Laboratory, Los Alamos, NM, USA*

²²*Centro de Investigación en Computación, Instituto Politécnico Nacional, México City, México.*

²³*Dept of Physics and Astronomy, University of New Mexico, Albuquerque, NM, USA*

²⁴*Universidad Autónoma del Estado de Hidalgo, Pachuca, México*

²⁵*Department of Physics, Temple University, Philadelphia, PA, USA*

²⁶*Instituto de Ciencias Nucleares, Universidad Nacional Autónoma de México, Ciudad de México, México*

²⁷*Department of Physics and Astronomy, University of Utah, Salt Lake City, UT, USA*

²⁸*Department of Physics, Sungkyunkwan University, Suwon 16419, South Korea*

ABSTRACT

The first TeV gamma-ray source with no lower energy counterparts, TeV J2032+4130, was discovered by HEGRA. It appears in the third HAWC catalog as 3HWC J2031+415 and it is a bright TeV gamma-ray source whose emission has previously been resolved as 2 sources: HAWC J2031+415 and HAWC J2030+409. While HAWC J2030+409 has since been associated with the *Fermi-LAT* Cygnus Cocoon, no such association for HAWC J2031+415 has yet been found. In this work, we investigate the spectrum and energy-dependent morphology of HAWC J2031+415. We associate HAWC J2031+415 with the pulsar PSR J2032+4127 and perform a combined multi-wavelength analysis using radio, X-ray, and γ -ray emission. We conclude that HAWC J2031+415 and, by extension, TeV J2032+4130 are most probably a pulsar wind nebula (PWN) powered by PSR J2032+4127.

Keywords: Gamma-ray sources (633); Pulsars (1301)

1. INTRODUCTION

First observed in 2005 by the High Energy Gamma Ray Astronomy (HEGRA) experiment, TeV J2032+4130 was the first very high energy (> 100 GeV) γ -ray source in the TeV range with no lower energy counterpart (Aharonian et al. 2005). TeV J2032+4130 is located in the *Fermi-LAT* Cygnus Cocoon region, a large extended source of GeV γ -ray emission that contains the Cygnus OB-2 star cluster (Ackermann et al. 2011). The extent of the original HEGRA detection was 0.11° and was comparatively dim to HEGRA’s detection of the Crab above 1 TeV at 5% of the Crab’s flux (Rowell et al. 2003; Aharonian et al. 2005).

Follow-up studies by the X-ray observatories Suzaku, Chandra, and XMM-Newton revealed significant diffuse non-thermal X-ray emission co-incident with TeV J2032+4130 (Murakami et al. 2011; Horns et al. 2007). In Murakami et al. (2011), they revealed two sub-structures, one of which was co-incident with the pulsar PSR J2032+4127, in addition to a large diffuse excess measured across TeV J2032+4130’s extent (Murakami et al. 2011). XMM-Newton’s detection is roughly the same size as TeV J2032+4130, though no sub-structures were found (Horns et al. 2007). Both measurements had fluxes significantly lower than that of the γ -ray source. Two hypotheses were proposed for the emission: hadronic, driven by pion decay, and leptonic, produced via a combination of synchrotron and inverse Compton scattering. Both hypotheses are considered in this analysis and are discussed in Section 5.

Radio observations made using the Very Large Array (VLA) revealed a large number of radio sources in the direction of TeV J2032+4130’s center of gravity (CoG). One of these sources was characterized by faint, non-thermal emission in roughly a half-circle around the CoG with a total area of ~ 27 arcmin² (Paredes et al. 2006; Marti et al. 2007). The region had an estimated energy

content of 6×10^{45} erg and seemed to indicate an efficient injector of nonthermal particles. Additionally, the semi-circular shape of the emission region seems to indicate an old supernova shell and is most likely the radio counterpart of TeV J2032+4130.

Later TeV observations by the Very Energetic Radiation Imaging Telescope Array System (VERITAS) in 2014 (Aliu et al. 2014) and 2018 (Abeysekara et al. 2018a) found emission that corresponded to an asymmetric Gaussian within the energy range 0.5-50 TeV. In both Aliu et al. (2014) and Abeysekara et al. (2018a), they hypothesize that the emission is from a pulsar wind nebula (PWN) and whose source is PSR J2032+4127. Furthermore, while they do not observe one, they predicted a cut-off near 10 TeV.

In the second (Abeysekara et al. 2017b) and third (Albert et al. 2020) catalogs published by the High-Altitude Water Cherenkov (HAWC) observatory, sources 2HWC and 3HWC J2031+415 are detected coincident with TeV J2032+4130. A follow-up dedicated analysis resolved two sources: HAWC J2031+415, which was associated with the probable PWN, and HAWC J2030+409, believed to be the TeV extension of the *Fermi-LAT* Cygnus Cocoon (Abeysekara et al. 2021a). Though that analysis focused on the Cygnus Cocoon (henceforth referred to as the Cocoon), it was found that HAWC J2031+415 had an extension of 0.27° and a power-law with exponential cut-off spectral model with a cut-off on the order of > 10 TeV and is consistent with VERITAS’ observations (Abeysekara et al. 2021a; Aliu et al. 2014).

As asserted by VERITAS, PSR J2032+4127 is most likely the power source for the PWN. PSR J2032+4127 is a rather unique pulsar to power a PWN. First, it is old at an estimated characteristic age of ~ 200 kyr with an estimated spin-down luminosity $\dot{E} = 1.5 \times 10^{35}$ erg/s. Current estimates have moved it from 3.8 kpc in Murakami et al. (2011) to 1.33 ± 0.06 kpc in the most recent pulsar catalog published by the Australian

Telescope National Facility (ATNF) (Manchester et al. 2005). This places it inside the Cocoon, which has a distance of ~ 1.4 kpc (Abeysekara et al. 2021a; Ackermann et al. 2011). Additionally, it is a long period binary with the $\sim 15 M_{\odot}$ star MT91 213 and has an orbital period of 50 years (Lyne et al. 2015). This makes the system unique, as TeV binary γ -ray pulsar systems are rare. While not originally associated with observed X-ray emission (Lyne et al. 2015), the pulsar is now believed to be responsible for it (Aliu et al. 2014) and will be considered for the multi-wavelength analysis presented in Section 5.

In this paper, we further study the probable PWN HAWC J2031+415. In Section 2, we introduce the HAWC observatory, Section 3 discusses the analysis pipeline that we use to describe HAWC J2031+415, and Section 4 explores the energy-dependent morphology of HAWC J2031+415. Section 5 incorporates data from other observatories to perform a multi-wavelength analysis on this source.

2. HAWC

The HAWC observatory is located on the extinct volcano Sierra Negra in Mexico. The detector is at an altitude of 4100 meters with a main array of 300 water Cherenkov detectors, covering an area of 22,000 m². Each detector has 4 photo-multiplier tubes (PMT), three 8 inch and one high quantum efficiency 10 inch. Further detector details can be found in Abeysekara et al. (2023). The recorded γ -ray events are divided into bins based on the fraction of PMTs hit in the event reconstruction (f_{hit}) (Abeysekara et al. 2017a). Additional algorithms incorporate the estimated energies of these events among other parameters in the reconstruction process. These are the neural network (NN) and the ground parameter (GP) algorithms (Abeysekara et al. 2019). The NN utilizes a dual-layer neural network to estimate the energies of incoming photons by using three general inputs: the amount of energy deposited, the amount the shower is contained in the detector’s footprint, and the attenuation degree caused by the atmosphere. The GP reconstructs the shower based on the charge density from a fixed distance to the shower core. We present results using the NN while the GP was used as a cross check.

3. SOURCE SEARCH AND SPECTRAL FITTING

3.1. Data Considered

For this analysis, approximately 2400 days of reconstructed data using the NN algorithm are used. This is approximately 1400 days more than the previous in-depth investigation into this region (Abeysekara et al.

2021a). Additionally, this new data set also utilizes updated reconstruction algorithms that offer better angular resolution and background rejection, particularly at higher energies (Albert et al. 2024). For the Region of Interest (ROI), a 6° circular region centered on ($l = 78.9^{\circ}$, $b = 1.6^{\circ}$) with a mask on 3HWC J2019+367 is selected, shown in Figure 1. As done in Abeysekara et al. (2021a), the mask on 3HWC J2019+367 is used to prevent potential contamination caused by the brightest source in the Cygnus Cocoon region.

3.2. Method

To fit the γ -ray data, we used both the Multi-Mission Maximum Likelihood framework (Vianello et al. 2015, 3ML)¹ and the HAWC Accelerated Likelihood (HAL)² (Abeysekara et al. 2022) plugin. This implementation allows extensive multi-source fitting for complex regions. The framework considers a test statistic (TS) that evaluates the statistical significance of a given model with a given number of free parameters. The TS is used to compare an alternative hypothesis with a null hypothesis. It is defined as

$$\text{TS} = 2 \ln \left(\frac{L_{\text{alt}}}{L_{\text{null}}} \right) \quad (1)$$

If two alternate nested hypotheses are compared, $\Delta\text{TS} = \text{TS}_2 - \text{TS}_1 = 2 \ln(L_2/L_1)$ can be used to determine which model is preferred (Abeysekara et al. 2017a). If the difference in free parameters between the models is 1, then Wilks’ theorem can be used to give a pre-trial significance that follows $\sigma = \sqrt{\text{TS}}$ (Wilks 1938).

To fully model the emission in the ROI, we performed a source search method similar to that of the *Fermi*-LAT extended source catalog (Ackermann et al. 2017). All models considered are from the *Astromodels*³ Python package. The first step is to fit a diffuse background emission (DBE) model with a power law (PL) spectral model. This model is described by

$$\frac{dN}{dE} = N_o \left(\frac{E}{E_p} \right)^{-\alpha}, \quad (2)$$

where N_o and α are the flux normalization and index for the source. E_p is the fixed pivot energy for the source and is selected to minimize the correlation between the flux normalization and index. The DBE model includes both the Galactic diffuse emission and any unresolved sources present. The index and pivot energy are fixed at

¹ <https://github.com/threeML/threeML>

² https://github.com/threeML/hawc_hal

³ <https://github.com/threeML/astromodels>

2.75 and 7 TeV respectfully, while the flux normalization is allowed to float. Additionally, this source is modelled as a band of emission along the Galactic plane with a radius of 1° .

With this done, a significance map, like what is shown in Figure 1, is made and the brightest point of emission is selected. A floating point source (PS) with a power law spectral model is then added near this point. The location and spectral parameters are floated to minimize the negative log-likelihood function.

Once this fit is complete, the Δ TS between the first alternate hypothesis (in this case the DBE fit) and the second (DBE + 1 PS) is considered. If Δ TS < 25, the method concludes with a final model. If Δ TS > 25, then a new PS is added to the next highest point of significance. This process repeats until the Δ TS < 25 threshold is achieved.

After the PS portion of the search is completed, the extension of each source is tested. The extended model (EXT) considered is a symmetric Gaussian and is given by

$$\frac{dN}{d\Omega} = \left(\frac{180}{\pi}\right)^2 \frac{1}{2\pi\sigma^2} \exp\left(-\frac{\bar{\theta}^2}{2\sigma^2}\right), \quad (3)$$

where $\bar{\theta}$ and σ are the angular distance and width of the Gaussian respectively. As with the previous step, a Δ TS comparison is considered, this time between the PS and EXT models. If Δ TS < 25, then the PS model is preferred and if Δ TS > 25, the extension is kept. The most significant point source is made an extended source and has both its location and spectral parameters free. If the Δ TS > 25 threshold is met, then both the extension is kept and, if any point sources now have Δ TS < 25, they are dropped. This repeats for all remaining point sources. Once this step is complete, the whole region is refitted and the final source location(s) and extension(s) are given.

Once the source model has been completed, the spectrum of each source is tested. This is done by considering three models, the power law model shown in Equation 2, a power law with an exponential cut-off (PLC) shown in Equation 4, and a log parabola (LP) given by Equation 5 below.

$$\frac{dN}{dE} = N_o \left(\frac{E}{E_p}\right)^{-\alpha} \exp\left(-\frac{E}{E_c}\right) \quad (4)$$

$$\frac{dN}{dE} = N_o \left(\frac{E}{E_p}\right)^{-\alpha-\beta \ln(E/E_p)} \quad (5)$$

The extra terms E_c and β are the cut-off energy and curvature of the spectrum decay respectively. Given the

un-nested nature of the spectral models, the Bayesian Information Criterion (BIC) is used and is given by (Wit et al. 2012)

$$\text{BIC} = k \ln(n) - 2 \ln(\hat{L}) \quad (6)$$

The BIC adds a term that penalizes more complex models given by the k number of parameters for a given likelihood \hat{L} and number of events n . A Δ BIC > 2 for $L_1 - L_2$ indicates that L_2 is preferred.

3.3. Results

Once the source search process has been completed, the final source model contains the following: DBE and three extended sources and is in agreement with Abeysekara et al. (2021a). Two sources correspond to HAWC J2030+409 and HAWC J2031+415 and HAWC J2030+409 is associated with the *Fermi*-LAT Cygnus Cocoon (Ackermann et al. 2017) while HAWC J2031+415 is near co-incident with TeV J2032+4130 and is asserted in this work to be a PWN.

The third extended source, corresponding to 3HWC J2020+403, was previously found in Fleischhack (2019) and Abdollahi et al. (2020) to be associated with the supernova remnant Gamma Cygni. There, its model was found to be a disk rather than a symmetric 2D Gaussian. For a disk model, the emitted flux is held constant over a fixed radius rather than decreasing radially with a 2D Gaussian. We tested this by creating a disk model with a fixed radius of 0.63° as found by Fleischhack (2019); Abdollahi et al. (2020) and the whole model was refitted. The result was a negligible difference in TS (Δ TS < 1) and, while the Gaussian model is used for this analysis, a dedicated work on 3HWC J2020+403 is need to determine its true morphology.

The results from the fitting process are given in Table 1 and the preferred spectral models for the sources being as follows: HAWC J2031+415 is a PLC, HAWC J2030+409 is a LP, and 3HWC J2020+403 is a PL. Additionally, the DBE model is included in the final fit with its flux normalization being fitted. A brief comparison to the previously published work is discussed in Section 3.4.

The systematic uncertainties given in Table 1 are found by performing a series of fits with detector response files that describe different detector configurations. Further details are given in Abeysekara et al. (2019) and are briefly summarized here. These response files are generated assuming different PMT response to showers (efficiency over time, response, etc) and are then compared to HAWC's standard response file. The fitting process is then repeated with these new response files, the difference between the new fit values and those in

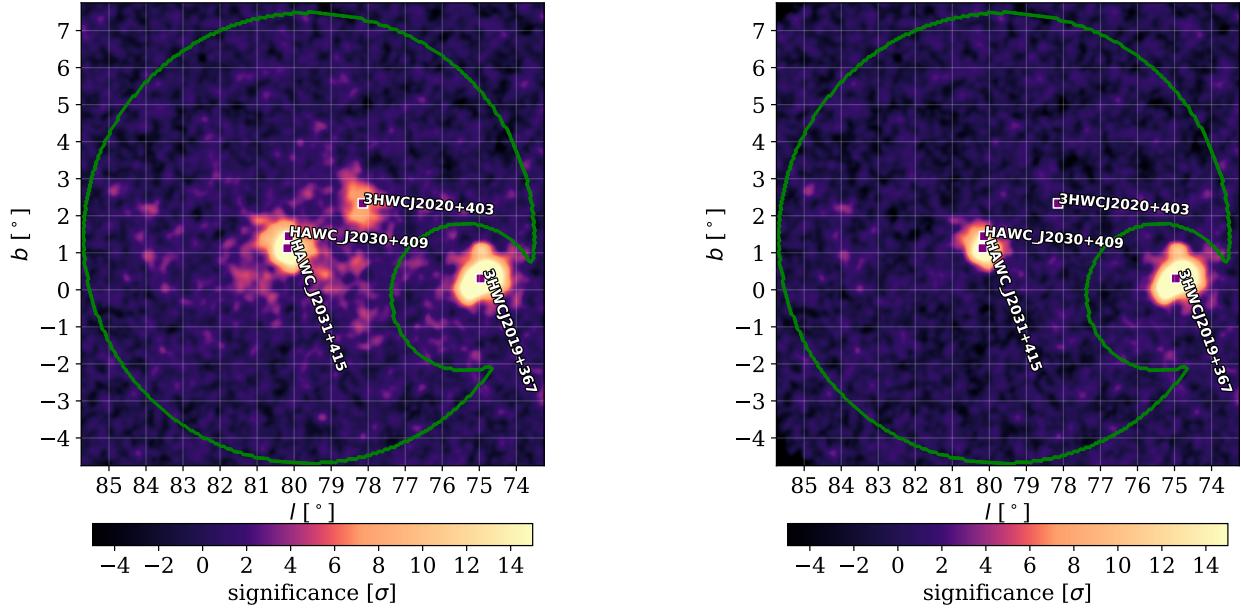


Figure 1. LEFT: the significance map of the ROI with the source associations found in Section 3. A mask is placed on 3HWC J2019+367 to avoid contamination from its emission for this analysis. RIGHT: HAWC J2031+415’s emission is shown after contributions from HAWC J2030+409 and 3HWC J2020+403 were subtracted from the data map.

Source Name	Spectral Parameters	Morphology
HAWC J2031+415	$\phi_{4.9 \text{ TeV}} = 1.29^{+0.14+0.15}_{-0.12-0.25} \times 10^{-13}$ $\alpha = 1.94^{+0.10+0.10}_{-0.10-0.19}$ $E_c = 32^{+7+5}_{-7-4}$	$\sigma = 0.255^{+0.016+0.015}_{-0.016-0.019}$ RA = $307.92^{+0.02+0.01}_{-0.02-0.01}$ Dec = $41.48^{+0.02+0.01}_{-0.02-0.01}$
HAWC J2030+409	$\phi_{4.2 \text{ TeV}} = 1.1^{+0.12+0.20}_{-0.11-0.09} \times 10^{-12}$ $\alpha = 2.59^{+0.07+0.08}_{-0.07-0.18}$ $\beta = 0.11^{+0.04+0.02}_{-0.04-0.05}$	$\sigma = 2.50^{+0.26+0.25}_{-0.26-0.48}$ RA = $307.54^{+0.22+0.10}_{-0.22-0.24}$ Dec = $41.64^{+0.24+0.10}_{-0.24-0.31}$
3HWC J2020+403	$\phi_{1.1 \text{ TeV}} = 4.3^{+0.8+0.6}_{-0.7-0.3} \times 10^{-12}$ $\alpha = 2.91^{+0.07+0.04}_{-0.07-0.09}$	$\sigma = 0.36^{+0.05+0.03}_{-0.05-0.02}$ RA = $305.05^{+0.07+0.05}_{-0.07-0.03}$ Dec = $40.52^{+0.05+0.03}_{-0.05-0.03}$
DBE	$\phi_{7 \text{ TeV}} = 2.9^{+1.1+3.4}_{-0.8-1.1} \times 10^{-12}$ $\alpha = 2.75$ (fixed)	$\sigma = 1$ (fixed)

Table 1. Fit results from the systematic source search. The first uncertainty listed is statistical and the second is systematic. The units are as follows: ϕ_{E_p} is the flux normalisation with units $1/(\text{TeV cm}^2 \text{ s})$; RA, Dec, and σ are given in degrees; and E_c has units of TeV. E_p was found for each source independently.

Table 1 are found, and then are added in quadrature to produce the total systematic uncertainties.

We determine the energy range of each source using the following procedure as is the same as in [Abeysekara et al. \(2017\)](#). Each spectral model is independently multiplied by a step function that models an abrupt cut-off in the spectrum. The only free parameters are the cut-off values; all other parameters are fixed at their best

fit values. These values float until the TS of significance of the sources drops by 1σ . This gives the 1σ energy limits for the sources as follows in units of TeV: 0.4-151 for HAWC J2031+415, 0.5-250 for HAWC J2030+409, and 0.26-100 for 3HWC J2020+403.

With the multi-source fitting process complete, we then isolate the emission of HAWC J2031+415 by subtracting out the modelled emission of the DBE,

HAWC J2030+409, and 3HWC J2020+403 from Figure 1 LEFT. The result is shown in Figure 1 RIGHT.

Figure 2 shows the SED of HAWC J2031+415 compared to selected other observations. These observations represent the most current detections of TeV J2032+4130 from their respective observatories. It can be seen that HAWC’s observation is in tension with all other observations. This can be explained by HAWC J2031+415’s much larger extension compared to previous studies. For example, in HEGRA’s initial discovery, TeV J2032+4130 had an extent of 0.11° compared to this work’s 0.26° , thus leading to a much larger flux. Of special note is the scaling done to VERITAS’s measurement. We follow the procedure outlined in Albert et al. (2021).

The spectrum reported by VERITAS was found from a smaller region than the full observed region presented in Abeysekara et al. (2018a). VER J2031+415’s morphology is described as an asymmetric Gaussian with extents $0.15 \pm .03^\circ$ and $0.07 \pm 0.01^\circ$ for the semi-major and semi-minor axes with a 63° rotation to the northwest. By contrast, the flux calculation uses a circular region with radius 0.23° centered on VER J2031+415. This method is different to what is used in this analysis where the flux calculation is computed concurrently with the morphological fit. As such, the flux measurements of VERITAS and HAWC may be systematically offset for larger extended sources like HAWC J2031+415. To account for this offset, the flux reported by VERITAS is scaled by assuming a larger integration region. This gives a scaling factor of 1.49 and is used in Figure 2.

3.4. Comparison to Previous Work

This work found identical (within uncertainties) morphological and spectral models for HAWC J2031+415 and 3HWC J2020+403 as in Abeysekara et al. (2021a) but there is tension with HAWC J2030+409’s spectral model. In Abeysekara et al. (2021a), the preferred model was a power law with $\phi_{4.2 \text{ TeV}} = 9.3_{-0.8-1.23}^{0.9+0.93} \times 10^{-13} \text{ TeV}/(\text{cm}^2\text{s})$ and $\gamma = 2.64_{-0.05-0.03}^{+0.05+0.09}$ while this work found a log parabola model to be strongly preferred with $\Delta\text{BIC} = 19$. This is explained by the superior background rejection utilized with the newer data set that reveals a curvature at the highest energies. The spectral and morphological fits for HAWC J2031+415 and 3HWC J2020+403 are comparable to Abeysekara et al. (2021a). One additional note is the recently published LHAASO result of the Cygnus region (LHAASO Collaboration 2024) where they find a PL spectral model for HAWC J2030+409. An in-depth comparison is beyond the scope of this work, but broadly the two models are compatible within systematic uncertainties.

4. ENERGY-DEPENDENT MORPHOLOGY STUDY

4.1. Methodology

In order to study any possible energy-dependent morphology of HAWC J2031+415, we utilized the method described in Albert et al. (2021); Joshi (2019). This method uses the longitudinal profiles of discrete energy bands over the source to count the number of excess events observed. Six energy bands are selected in TeV units: 0.3-1.0, 1.0-3.2, 3.2-10, 10-32, 32-100, and 100-316.

The longitudinal profile region is defined as a rectangle of dimensions 6° long by 1° centered at the pulsar’s location with HAWC J2030+409, 3HWC J2020+403, and the DBE subtracted out. Furthermore, the rectangle is rotated by 15° to lie on the line connecting HAWC J2031+415’s centroid and PSR J2032+4127 in Galactic coordinates. This is to determine whether the observed emission trends toward the pulsar’s location with changing energy. This can be seen in Figure 3.

To determine the true size of the extended emission in each energy band, the following procedure is used. First, the rectangular regions is divided into 50 bins, each with a width of 0.12° . Then the excess counts of each bin are summed and plotted. This is shown by the data points in Figure 4. To measure the intrinsic width of the extension, a 1D Gaussian is fit to each band, as indicated by the red lines in Figure 4. However, as discussed in Abeysekara et al. (2021b) and Joshi (2019), there is a smearing effect caused by point sources not appearing point-like with this method.

To rectify this, a point source with HAWC J2031+415’s index of 1.94 is simulated at PSR J2032+4127’s location. This simulated source is then handled in the same method described above. The 1D Gaussians found with the simulated source are the “smearing” effect and are shown by the dashed blue line in Figure 4. This effect can now be subtracted out in quadrature with the observed data fits.

4.2. Results

From Figure 4, there are no significant detections in bands 1 and 6; this is most likely caused by the spectrum of HAWC J2031+415. This source is not significantly detected in GeV or high TeV energies, which is what these two bands primarily comprise of. While there are fits for all other bands, band 2 requires more investigation. Its fit is diffuse and was checked against the diffuse background emission model to ensure the observed emission was from HAWC J2031+415 and not a large background fluctuation. The emission is observed at a 5σ level and is confirmed as a positive detection of

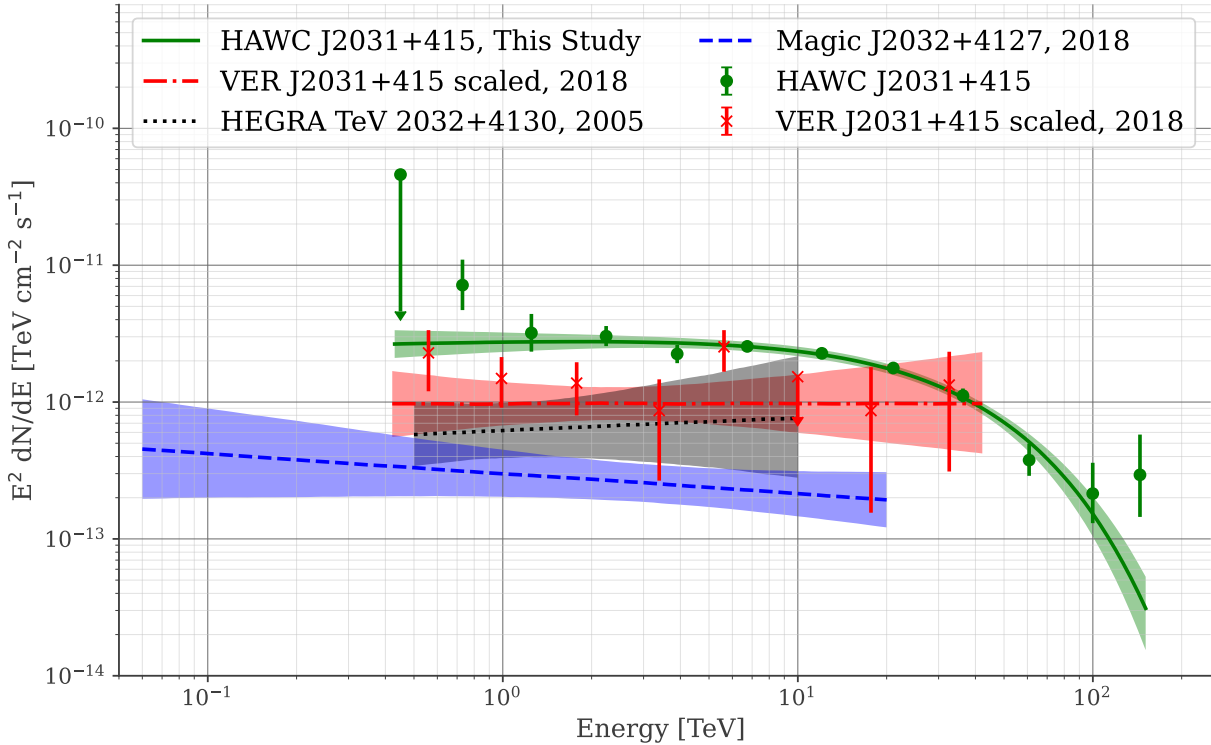


Figure 2. SED of HAWC J2031+415. The other observations are from Aharonian et al. (2005); Albert et al. (2008); Abeysekara et al. (2018b,a) respectively and were selected as the most current independent observations available. Additionally, all uncertainties are statistical only

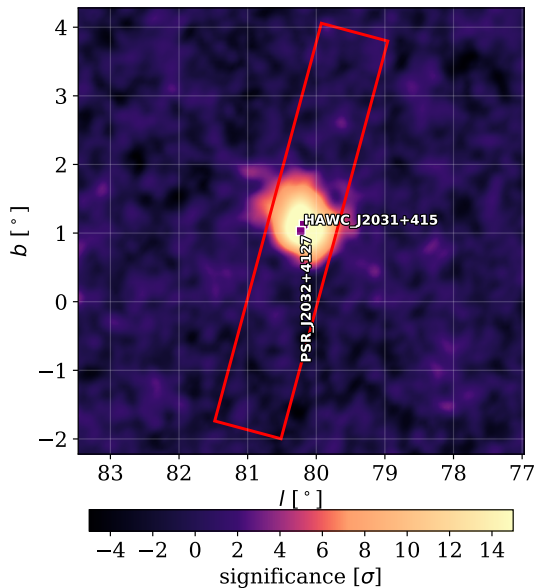


Figure 3. The significance map used for the energy morphology study. The rectangle highlights the longitudinal profile region used for the energy-dependent morphology study.

HAWC J2031+415. Bands 3, 4, and 5 all show significant detections.

Figure 5 shows the size of TeV emission with increasing energy and its location with respect to PSR J2032+4127. The size is the true width of emission after subtracting both the point source smearing and any systematic offsets between data and simulation. This true width is given by

$$\sigma_{\text{true}} = \sqrt{\sigma_{\text{fit}}^2 - (\sigma_{\text{sim}} + \sigma_{\text{offset}})^2} \quad (7)$$

While some faint energy-dependent morphology is present, particularly in the morphology shift from bands 2 to 3, there is no discernible trend at higher energies. Likewise, while there is a faint trend towards the pulsar's location at lower energies, there is nothing conclusive at higher energies.

5. MULTI-WAVELENGTH FITTING

5.1. *NAIMA* Framework

The Naima software is a non-thermal modelling framework that utilizes Markov chain Monte Carlo calculations (Zabalza 2015). It has both leptonic and hadronic models that take flux points like the ones shown in Figure 2 as inputs and fits different emission models to them. At the γ -ray regime, the leptonic model consid-

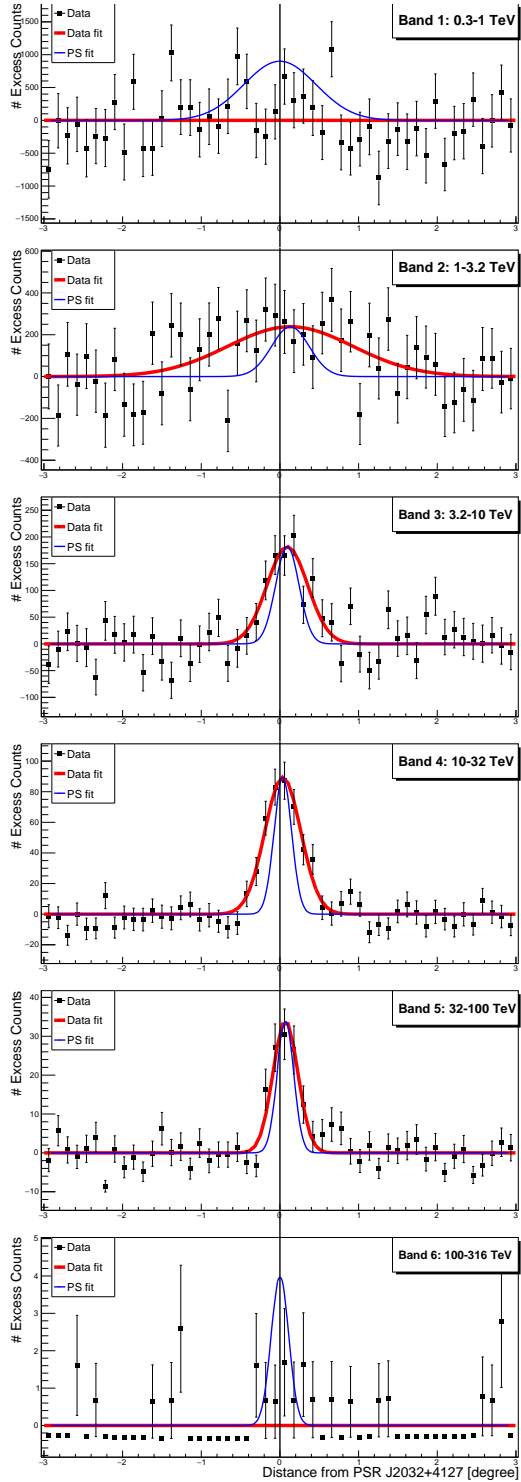


Figure 4. The longitudinal profiles for the excess count maps for HAWC J2031+415. The red fitted lines correspond to the fitted Gaussians of each band while the blue dashed lines are the simulated point source Gaussians discussed in Section 4. The location of PSR J2032+4127 is indicated by the vertical line. The distance between HAWC J2031+415’s best fit centroid location and the pulsar’s location is 0.13° or about 3 pc.

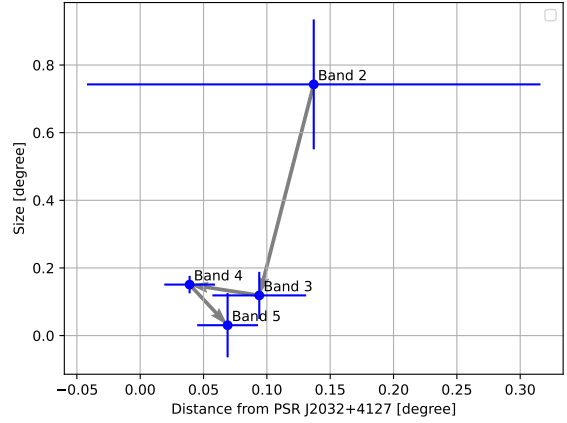


Figure 5. The results from the energy morphology study as described in Section 4. HAWC J2031+415’s true size is presented on the y-axis and the distance to the pulsar is on the x-axis.

ers inverse Compton (IC) scattering of relativistic electrons off low energy photons and at the X-ray regime considers synchrotron emission released by high energy electrons moving through magnetic fields. The hadronic model considers π^0 decay (PD) from proton-proton collisions. These models can be combined together and are discussed further below.

5.2. Methodology

For the data set, we consider the X-ray observations from Suzaku (Murakami et al. 2011) and XMM-Newton (Horns et al. 2007) along with the radio detection by VLA (Paredes et al. 2006) as discussed in Section 1 in addition to the flux points shown in Figure 2. Regarding the Suzaku fluxes, we consider the diffuse X-ray emission measured across HEGRA’s TeV detection region and scale it by a factor of 6.7 in the same manner as VERITAS’s data discussed in Section 3. Likewise, the XMM-Newton data is scaled as well. This scaling assumes that the X-ray flux is constant across HAWC’s detection range. Additionally the TeV data from VERITAS shown in Figure 2 is also considered. Though its measured flux is systematically lower, VERITAS’s superior sensitivity to high GeV and low TeV energies adds a crucial lower energy component to HAWC’s flux measurement.

The analysis of Suzaku’s detection is based on a distance of 3.6 kpc but as previously discussed recent studies have placed the pulsar at a distance of 1.33 kpc (Manchester et al. 2005). This updated distance will be used. Additionally, they assumed the main photon field being scattered to be from the Cosmic Microwave

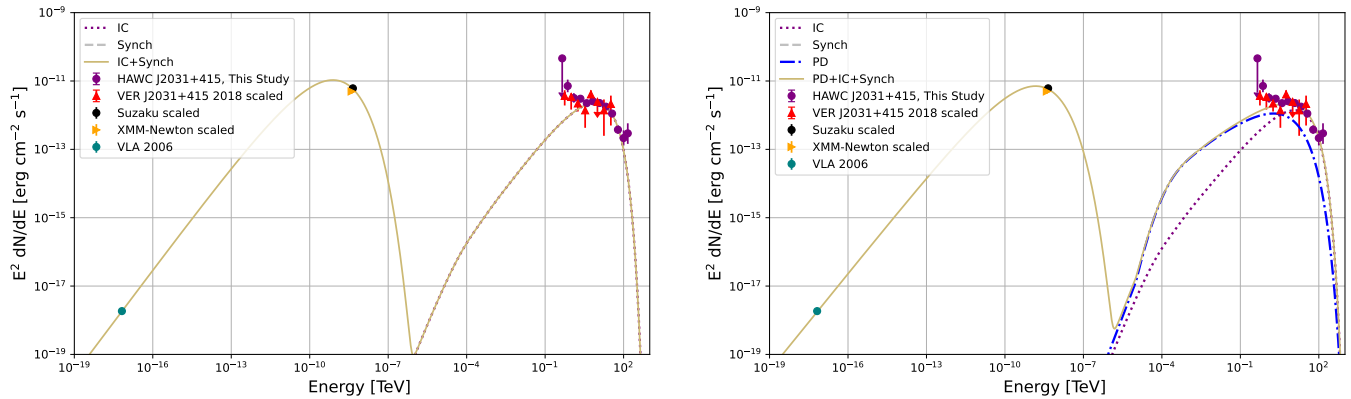


Figure 6. Leptonic (LEFT) and lepto-hadronic (RIGHT) emission modelling based on multi-wavelength data. Note that Suzaku, XMM-Newton, and VERITAS fluxes are scaled as discussed in Section 5.

Model	$\log(\phi)(1/\text{TeV})$	E_p (TeV)	α	E_c (TeV)	$B(\mu\text{G})$	$W_{e,p} > 1\text{TeV}$ (erg)	BIC
Leptonic	42.64 ± 0.09	20	1.00 ± 0.04	27 ± 13	5.9 ± 0.39	$(3.4 \pm 0.3) \times 10^{45}$	67.9
Lepto-	41.96 ± 0.14	20	1.21 ± 0.05	55 ± 6	6.2 ± 0.08	$(1.5 \pm 0.3) \times 10^{45}$	77.3
Hadronic	42.77 ± 0.07	20	1.22 ± 0.07	95 ± 22	—	$(1.6 \pm 0.3) \times 10^{46}$	

Table 2. The fit values that correspond to the fitting process discussed in Section 5. All uncertainties presented are statistical only.

Background (CMB), though they note the model is most likely more complex.

To model the observed X-ray and TeV emission, we consider two emission mechanisms: leptonic and lepto-hadronic. For the pure leptonic emission hypothesis, we model a combination of synchrotron and IC. For the lepto-hadronic case, PD is included with the leptonic contributions. If PD is preferred, there should be heavy suppression of IC in the TeV regime. The proton density considered was found by considering the column density of $7.7 \times 10^{21} \text{cm}^{-2}$ found in (Camilo et al. 2009) and dividing by HAWC’s observed extent of ~ 5.9 pc to get a density of 417 protons per cm^{-3} . The fit results are shown in Figure 6 and are given in Table 2.

For both models, cut-off power spectrums are assumed for proton and electron populations. This comes from observed flux points for HAWC J2031+415 and its best-fit spectral model. The parameters are the same as in Equation 4 with E_p being set to 20 TeV for both models. Additionally, the energies required for the two models are given as W_e for leptonic and both W_e and W_p for lepto-hadronic.

5.3. Leptonic Scenario

The X-ray observations from Suzaku and XMM-Newton both note that the observed X-ray flux is significantly lower than that of HEGRA’s observation. As such, this would constrain the ambient magnetic field in the PWN to be in the order of a few μG if the TeV emis-

sion is leptonic in origin. Additionally, there would have to be a sharp cut-off of the electron energy distribution in the few 10’s of TeV. If the TeV electron spectrum cuts off sharply, then the X-ray flux would decrease and could explain the much smaller X-ray to γ -ray fluxes measured (Murakami et al. 2011). From Table 2 and the energy range studies discussed in 3, it can be seen that HAWC’s observations match these hypotheses.

Two assumptions used in this analysis require additional explanation. The first would be the scaling used for the Suzaku and XMM-Newton observations. The scaling process assumed that the observed X-ray flux can be extended across HAWC J2031+415’s size, similar to the VERITAS scaling. This was done to extrapolate an approximate X-ray flux assuming the actual X-ray emission region is comparable to HAWC’s TeV emission. Preliminary findings from LHAASO (Li 2022) also indicate a TeV emission region of $0.24 \pm 0.03^\circ$ so additional X-ray observations targeting a wider field of view are needed to see if an updated extended source matches current TeV observations. As such, the magnetic field we present should be treated as a lower limit.

The second assumption regards the scattering medium used. This analysis assumes the medium is a combination of the CMB, the far infrared (FIR), and near infrared (NIR). The energy densities were taken from Figure 9a in Popescu et al. (2017) with an assumed distance of 1 kpc, which is comparable to the distance of HAWC

J2031+415 at 1.33 kpc. Given that HAWC J2031+415 is in the Cygnus Cocoon, the scattering medium could be more complicated and more complete models may be required.

Another consideration is the energy budget E_T of PSR J2032+4127 and the relationship it has with the observed electron population. An approximation of E_T can be found by multiplying $\dot{E} = 1.5 \times 10^{35}$ erg/s by the pulsar’s characteristic age of ~ 200 kyr to give an energy budget of $\sim 9 \times 10^{47}$ erg (see. [H.E.S.S. Collaboration et al. \(2018\)](#)). While the E_T found is most probably lower than the actual energy budget, a comparison can still be drawn between W_e and the observed E_T and reveals that W_e is $\sim 1\%$ that of the energy budget for PSR J2032+4127. This value is reasonable ([Di Mauro et al. 2019](#)) and indicates that PSR J2032+4127 is capable of producing the observed electron population.

Additional GeV γ -ray data was considered but as of the writing of this paper, there are no other GeV sources besides PSR J2032+4127 ([Abdollahi et al. 2020](#); [Aliu et al. 2014](#)). Another note is the radio observations considered. While faint non-thermal diffuse emission was detected coincident with HAWC J2031+415 and may be its radio counterpart, no follow-up studies have concluded whether this is the case. More observations in both X-ray and radio bands are needed to better constrain the synchrotron emission and ambient magnetic field.

Lastly, the low energy electrons producing the synchrotron emission could be a separate population from the TeV emission HAWC sees. This 2-zone model was tested but lacked sufficient low energy data to confirm whether this scenario is preferred. Like with the combined model presented, more detected low energy observations of this specific region are required.

5.4. Hadronic Scenario

Considering lepto-hadronic production, the observed X-ray and HEGRA γ -ray emissions have been shown ([Horns et al. 2007](#)) to be explained by a “PeVatron” accelerator (accelerating to PeV energies) with B field constraints enforced by the diffuse X-ray emission. Recent observations from LHAASO ([Cao et al. 2021](#)) have reported that LHAASO J2032+4102 emitted a 1.4 PeV photon and so a known PeVatron accelerator is in this region. However, a follow-up paper analyzing the different LHAASO PeVatron sources ([de Oña Wilhelmi et al. 2022](#)) concluded that the low spin-down luminosity $\dot{E} = 1e35$ erg/s of PSR J2032+4127 is insufficient to produce such a photon. This photon could have come from the broader Cocoon as it has been shown ([Abeysekara et al. 2021a](#)) to produce PeV γ -rays.

Other considerations would be the source of the synchrotron emission and the behavior of the TeV γ -ray spectrum if the emission is lepto-hadronic in nature. If the emission is lepto-hadronic, then the observed synchrotron emission could be from a secondary population of electrons produced by π^\pm decay or be a primary low-energy population. While such a scenario has been tested, more low energy data is needed before any conclusions can be drawn.

One last consideration would again be the energy budget. The energy required for the observed proton population is found to be $W_p = 3.5 \times 10^{46}$ and is $\sim 7\%$ that of E_T . Recalling to when E_T was calculated, it should be treated as a lower limit to the energy budget and more extensive modelling is needed to fully constrain E_T . Like with the leptonic model, this is a reasonable percentage of the total energy budget. Though several key factors like lower energy X-ray emission and a high energy γ -ray extension are missing, further studies are needed to rule out this lepto-hadronic emission scenario.

5.5. Scenario Comparison

Both the leptonic and lepto-hadronic models fit the data well. One note is that, when the hadronic component is added to the leptonic model, it becomes suppressed at higher energies while IC dominates (see Fig 6), effectively making it a leptonic model. This, in addition to a Δ BIC of 22, indicates that the lepto-hadronic model is significantly dis-favored compared to the leptonic scenario. While this may indicate a statistical conclusion, it should be noted that BIC is heavily dependent on the number of data points being significantly larger than the amount of parameters being fitted. For this analysis, while the amount of data points is larger than the number parameters, more data is needed to conclusively say statistically which model is favored.

6. CONCLUSIONS

The morphological studies we presented here reveal HAWC J2031+415 to be an extended emission region modelled as a symmetric Gaussian. As predicted by [Aliu et al. \(2014\)](#) and [Abeysekara et al. \(2018a\)](#), it has a spectral shape of a power law with exponential cut-off energy $E_c = 19$ TeV, indicating that it may be a PWN. Given its close proximity to TeV J2032+4130, HAWC J2031+415 is most probably the high energy extension of this unidentified source. While there is no clear evidence for energy-dependent morphology (although a trend is present), the spectral shape matches that of a typical PWN.

We performed a multi-wavelength analysis considering both leptonic and lepto-hadronic emission hypotheses.

From X-ray data collected by Suzaku and XMM-Newton studies, a power law with exponential cut-off spectrum model was fitted. For the leptonic case, a fitted value of $5.9 \mu\text{G}$ for the ambient magnetic field and cut-off energy of $\sim 27 \text{ TeV}$ were found, matching the leptonic emission characteristics predictions put forth by both X-ray studies. Additionally, the observed energy to total energy budget of $\sim 1\%$ falls in line with other PWN. The results from the lepto-hadronic model are currently inconclusive but, while more studies are needed, the suppression of the hadronic component indicates that a pure leptonic model is favored. The leptonic emission result favors emission from HAWC J2031+415 and, by extension, TeV J2032+4130 to be produced by a pulsar wind nebula powered by PSR J2032+4127.

7. ACKNOWLEDGMENTS

We acknowledge the support from: the US National Science Foundation (NSF); the US Department of Energy Office of High-Energy Physics; the Laboratory Directed Research and Development (LDRD) program of Los Alamos National Laboratory; Consejo Nacional de Ciencia y Tecnología (CONACyT), México, grants 271051, 232656, 260378, 179588, 254964,

258865, 243290, 132197, A1-S-46288, A1-S-22784, CF-2023-I-645, cátedras 873, 1563, 341, 323, Red HAWC, México; DGAPA-UNAM grants IG101323, IN111716-3, IN111419, IA102019, IN106521, IN114924, IN110521, IN102223; VIEP-BUAP; PIFI 2012, 2013, PROFOCIE 2014, 2015; the University of Wisconsin Alumni Research Foundation; National Research Foundation of Korea (RS-2023-00280210); the Institute of Geophysics, Planetary Physics, and Signatures at Los Alamos National Laboratory; Polish Science Centre grant, DEC-2017/27/B/ST9/02272; Coordinación de la Investigación Científica de la Universidad Michoacana; Royal Society - Newton Advanced Fellowship 180385; Generalitat Valenciana, grant CIDEAGENT/2018/034; The Program Management Unit for Human Resources & Institutional Development, Research and Innovation, NXPO (grant number B16F630069); Coordinación General Académica e Innovación (CGAI-UdeG), PRODEP-SEP UDG-CA-499; Institute of Cosmic Ray Research (ICRR), University of Tokyo. H.F. acknowledges support by NASA under award number 80GSFC21M0002. We also acknowledge the significant contributions over many years of Stefan Westerhoff, Gaurang Yodh, and Arnulfo Zepeda Domínguez, all deceased members of the HAWC collaboration. Thanks to Scott Delay, Luciano Díaz and Eduardo Murrieta for technical support.

REFERENCES

- Abdollahi, S., et al. 2020, *The Astrophysical Journal Supplement Series*, 247, 33
- Abeysekara, et al. 2017a, *The Astrophysical Journal*, 843, 39
- Abeysekara, et al. 2022, in *37th International Cosmic Ray Conference*.
- Abeysekara, A., et al. 2017b, *The Astrophysical Journal*, 843, 40
- Abeysekara, A., Archer, A., Aune, T., et al. 2018a, *The Astrophysical Journal*, 861, 134
- Abeysekara, A., et al. 2018b, *The Astrophysical Journal Letters*, 867, L19
- . 2019, *The Astrophysical Journal*, 881, 134
- . 2021a, *Nature astronomy*, 5, 465
- Abeysekara, A., Albert, A., Alfaro, R., et al. 2023, *Nuclear Instruments and Methods in Physics Research Section A: Accelerators, Spectrometers, Detectors and Associated Equipment*, 1052, 168253, doi: <https://doi.org/10.1016/j.nima.2023.168253>
- Abeysekara, A. U., et al. 2017, *Science*, 358, 911, doi: [10.1126/science.aan4880](https://doi.org/10.1126/science.aan4880)
- Abeysekara, A. U., Albert, A., Alfaro, R., et al. 2021b, in *Proceedings of 37th International Cosmic Ray Conference — PoS(ICRC2021)*, Vol. 395, 836, doi: [10.22323/1.395.0836](https://doi.org/10.22323/1.395.0836)
- Ackermann, et al. 2017, *The Astrophysical Journal*, 843, 139
- Ackermann, M., et al. 2011, *science*, 334, 1103
- Aharonian, F., et al. 2005, *Astronomy & Astrophysics*, 431, 197
- Albert, A., et al. 2020, *The Astrophysical Journal*, 905, 76
- . 2021, *The Astrophysical Journal*, 911, 143
- Albert, A., Alfaro, R., Alvarez, C., et al. 2024, arXiv preprint [arXiv:2405.06050](https://arxiv.org/abs/2405.06050)
- Albert, J., et al. 2008, *The Astrophysical Journal*, 675, L25
- Aliu, E., et al. 2014, *The Astrophysical Journal*, 783, 16
- Camilo, F., Ray, P. S., Ransom, S. M., et al. 2009, *The Astrophysical Journal*, 705, 1
- Cao, Z., et al. 2021, *Nature*, 594, 33
- de Oña Wilhelmi, E., López-Coto, R., Amato, E., & Aharonian, F. 2022, *The Astrophysical Journal Letters*, 930, L2

- Di Mauro, M., Manconi, S., & Donato, F. 2019, *PhRvD*, 100, 123015, doi: [10.1103/PhysRevD.100.123015](https://doi.org/10.1103/PhysRevD.100.123015)
- Fleischhack, H. 2019, in 36th International Cosmic Ray Conference
- H.E.S.S. Collaboration, Abdalla, H., Abramowski, A., et al. 2018, *A&A*, 612, A2, doi: [10.1051/0004-6361/201629377](https://doi.org/10.1051/0004-6361/201629377)
- Horns, D., Hoffmann, A., Santangelo, A., Aharonian, F., & Rowell, G. 2007, *Astronomy & Astrophysics*, 469, L17
- Joshi, V. 2019, PhD thesis, Heidelberg University, Germany
- LHAASO Collaboration. 2024, *Science Bulletin*, 69, 449, doi: <https://doi.org/10.1016/j.scib.2023.12.040>
- Li, C. 2022, in 37th International Cosmic Ray Conference. 12-23 July 2021. Berlin, 843
- Lyne, A., et al. 2015, *Monthly Notices of the Royal Astronomical Society*, 451, 581
- Manchester, R. N., Hobbs, G. B., Teoh, A., & Hobbs, M. 2005, *The Astronomical Journal*, 129, 1993
- Marti, J., Paredes, J. M., Chandra, C. I., & Bosch-Ramon, V. 2007, *Astronomy & Astrophysics*, 472, 557
- Murakami, H., Kitamoto, S., Kawachi, A., & Nakamori, T. 2011, *Publications of the Astronomical Society of Japan*, 63, S873
- Paredes, J. M., Martí, J., Chandra, C. I., & Bosch-Ramon, V. 2006, *The Astrophysical Journal*, 654, L135
- Popescu, C., Yang, R., Tuffs, R., et al. 2017, *Monthly Notices of the Royal Astronomical Society*, 470, 2539
- Rowell, G., et al. 2003, in *International Cosmic Ray Conference*, Vol. 4, 2345
- Vianello, G., et al. 2015, arXiv preprint [arXiv:1507.08343](https://arxiv.org/abs/1507.08343)
- Wilks, S. S. 1938, *The Annals of Mathematical Statistics*, 9, 60, doi: [10.1214/aoms/1177732360](https://doi.org/10.1214/aoms/1177732360)
- Wit, E., Heuvel, E. v. d., & Romeijn, J.-W. 2012, *Statistica Neerlandica*, 66, 217
- Zabalza, V. 2015, arXiv preprint [arXiv:1509.03319](https://arxiv.org/abs/1509.03319)